ISSN 1330-3651 (Print), ISSN 1848-6339 (Online)
https://doi.org/10.17559/TV-20201222024536
Original scientific paper

Magnetic Field Analysis and Structure Optimization of Deflection Double Stator Switched Reluctance Generator

Zhe QIAN, Xueting WANG, Zheng LI*, Xuze YU

Abstract: The deterioration of environment, the aggravation of energy crisis and the exhaustion of non renewable energy promote the development of green new energy. Among them, wind power generation has become a research hotspot in the field of new energy at home and abroad. In this paper, the deflection double stator switched reluctance generator (DDSSRG) is taken as the research object, the basic modelling and analysis of DDSSRG are carried out, and the magnetic field of the generator is analyzed by using the finite element software. The structure of the generator is optimized by using the central composite design method (CCD). Finally, the experimental platform of the generator is built to verify the feasibility of the theory in structure.

Keywords: central composite design method (CCD); deflection double stator switched reluctance generator (DDSSRG); finite element software

1 INTRODUCTION

In the field of wind power generation, switched reluctance generator (SRG) has a strong competitive relationship with the traditional motor which can meet the demand of small and medium-sized power. With the development of switched reluctance motor, more and more topologies are studied. In reference [1], the C-core is used as the stator core, and the annular excitation auxiliary coil is clamped in the stator core to optimize the problem of large inductance limiting output power. However, due to the length of the air gap, there is a big difference between the measured maximum inductance and the calculated maximum inductance. In reference [2], the design, optimization and analysis of axial magnetic switched reluctance generator are carried out. Based on the radial magnetic field, the electromagnetic performance is studied. However, the calculation process of motor size is not described in detail. The size of the generator is obtained by combining with the magnetic finite element method in reference [3]. The tubular linear switched reluctance generator proposed in reference [4] can effectively improve the current carrying capacity and fault tolerance capability as wave energy conversion. However, how to improve the dynamic response and capture ability of wave energy conversion needs further study. The proposed SRG is analyzed by 3D finite element method, but the control strategy based on SRG is not discussed. In reference [5], the SRG model is established by using the flux linkage and torque data obtained by the finite element analysis method. According to the maximum power corresponding to the given wind turbine speed, the optimal turn on angle and turn off angle is calculated to maximize the efficiency.

With the continuous research of switched reluctance motor, reference [6-11] mentioned the optimization methods of switched reluctance motor, but these methods have their own limitations. The motor with double stator structure has the advantages of high precision, fast response, small torque ripple and high overload capacity, and its output characteristics are better than that of single stator structure motor [12-15], and it is widely used in the field of wind power generation [16-19]. However, due to the complex structure of double stator, compared with single stator SRM, the manufacturing process is complex, which will produce more iron loss and increase the loss [20], which needs further research and optimization.

In this paper, DDSSRG is proposed and its electromagnetic characteristics are studied. Compared with the traditional generator, it can work in worse conditions, and it can also run stably at high speed. Compared with the reluctance generator, it has higher operation efficiency.

2 WORKING PRINCIPLE OF GENERATOR

2.1 Generator Structure

The unique feature of DDSSRG is that it adopts double stator structure and increases deflection function. When the wind direction changes, it can still maintain high power generation efficiency. Fig. 1 shows the structure of the DDSSRG. The rotor is clamped in two stators. The angle between the center line of the outboard rotor and the center line of the inside rotor is 22.5°.

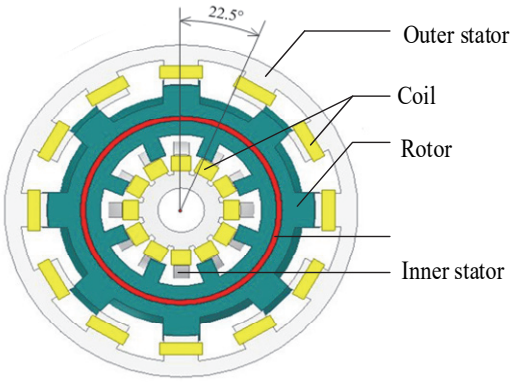

Figure 1 DDSSRG structure diagram

As can be seen from Fig. 1, the stator consists of two stators. In addition, the center lines of the two stator tooth poles are on the same straight line. The number of teeth poles of both is 12, C three-phase, inner stator winding is divided into D, E, F three-phase. The direction of current between two adjacent windings is opposite and the polarity is different. In the axial direction of the rotor, a good performance magnetic separator is set in the middle of the rotor yoke, which divides the rotor into two parts: the inner

part of the rotor and the outer part of the rotor, so as to prevent the mutual interference of the magnetic circuits on both sides. The tooth poles on both sides are staggered and the number of tooth poles is 8. The spherical structure of the stator and rotor of the generator can deflect in a certain space. The parameters of DDSSRG are in Tab. 1.

Table 1 Structural parameters of DDSSRG

Parameter	Value
Stator outer diameter /mm	320
Stator inner diameter /mm	44
Rotor inner diameter /mm	122
Rotor outer diameter /mm	253
Internal and external air gap /mm	0.5
Outer stator yoke height /mm	17.7
Yoke height of inner stator /mm	15.6
Rotor yoke height /mm	31.6
Core length /mm	73.8

2.2 DDSSRG Control Strategy

DDSSRG adopts the separate excitation mode to prevent the excitation voltage from being disturbed by the output voltage. Assuming that the prime mover drives the rotor to rotate at a certain speed, the on-off state of the power switch tube is judged by the output signal of the rotor position sensor, which ensures the continuous conversion of the excitation phase of the generator.

As shown in Fig. 2, the main power circuit of the generator is shown, in which Us is the external DC voltage source, S_1~S_6 are six on-off switches, and the conduction sequence is controlled by the trigger pulse of the driving circuit. When the switch is closed, the diodes VD_1,VD_2,VD_5,VD_6,VD_9 and VD_{10} ensure that the power supply in the excitation phase is supplied to the winding; when the switch is off, the diodes VD_3,VD_4,VD_7,VD_8,VD_{11} and VD_{12} provide free flow channel for the current in the winding. The pulse period of three-phase winding power switch device is 45° but the trigger pulse of each phase of inner stator lags 7.5° behind that of corresponding outer stator, so that when the center line of outer stator tooth pole coincides with that of rotor outer tooth pole, the center line of inner stator tooth pole coincides with that of inner rotor groove.

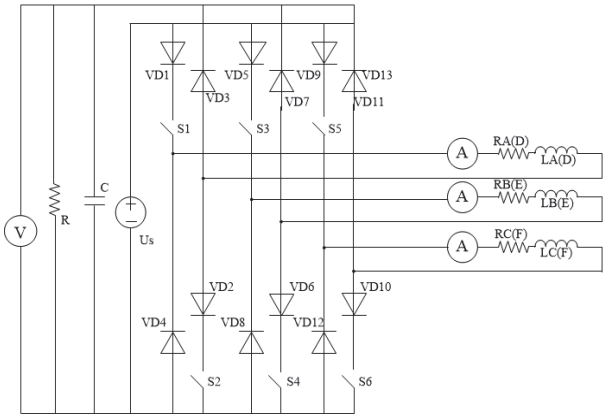

Figure 2 DDSSRG control circuit

In order to prevent the excitation voltage from being disturbed by the output voltage, it is assumed that the prime mover drives the rotor to rotate at a certain speed, and the on-off state of the power switch tube is judged by the output signal of the rotor position sensor, so as to ensure the continuous conversion of the excitation stage of the generator to the generation stage. Assuming that the prime mover drives the generator to rotate, the rotor speed is 200 r/min, the excitation voltage of the inner stator winding is 100 V, and the excitation voltage of the outer stator winding is 380 V. In this case, the transient simulation analysis of the generator is carried out and the following output characteristics are obtained.

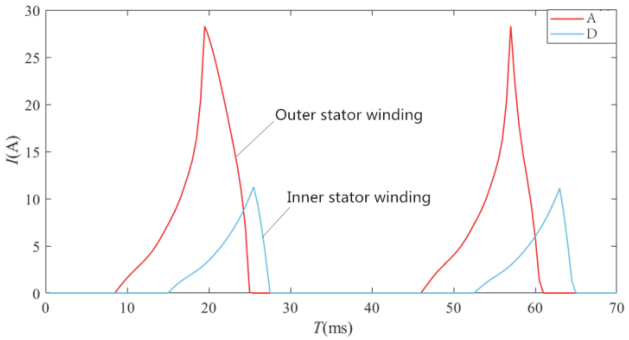

Figure 3 One phase current of stator winding

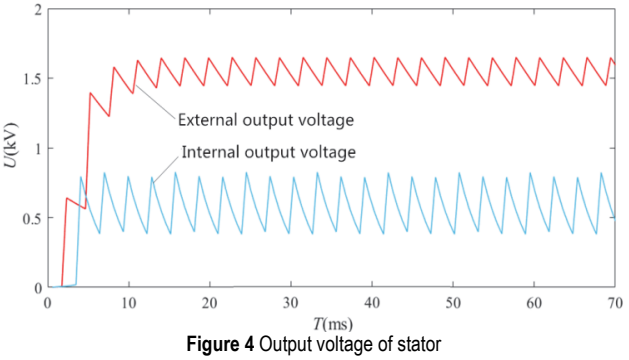

Figure 4 Output voltage of stator

As shown in Fig. 3, the current waveforms of phase *A* and phase *D* of the generator are similar triangular waves, but the amplitude difference is large. It is thus clear that the phase current amplitude of inner stator *D*-phase winding is about 12 A, and that of outer stator *A*-phase winding can reach 28 A, which is determined by the motor structure and different excitation voltage. In addition, the d-phase current is 6.25 ms later than the *A*-phase current in time. Fig. 4 shows the output voltage waveform of the generator. The internal output voltage fluctuates around 0.6 kV, and the outgoing output voltage can reach about 1.5 kV.

3 SIMULATION ANALYSIS OF DDSSRG

The electromagnetic analysis and calculation software are used to simulate it [21-22]. In order to further analyze the magnetic field performance of the generator, the electromagnetic simulation of the motor is carried out, and the two-dimensional magnetic field distribution diagram and magnetic flux density vector distribution diagram of the generator are obtained and analyzed.

In order to further study the operation characteristics of DDSSRG, it is necessary to analyze its magnetic field characteristics, such as the output voltage, current, working efficiency, torque ripple and other important performance indicators are bound up the magnetic field characteristics. Therefore, it is very important to analyze the magnetic field of DDSSRG.

3.1 Analysis of DDSSRG Magnetic Field

Fig. 5 shows the distribution of magnetic field lines in DDSSRG. As shown in the Fig. 5, the position of the rotor corresponds to the moment when θ = 10°, the winding phase A on the outer stator is in the opening moment, phase C is on, and phase B is in the cut-off state. At the same time, phase F of the upper winding of the inner stator is in the on state.

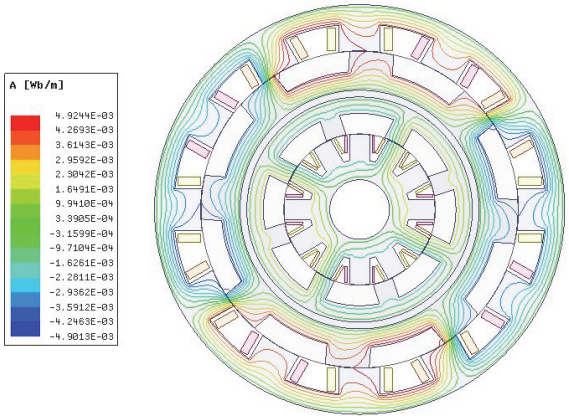

Figure 5 Distribution diagram of DDSSRG magnetic lines

There are alignment position, middle position and misalignment position in different positions of the rotor. Fig. 6 shows the distribution of magnetic force lines in three rotor positions. During the change of rotor position from non aligned position to aligned position, the main magnetic flux of the core increases gradually, and the air gap magnetoresistance decreases gradually.

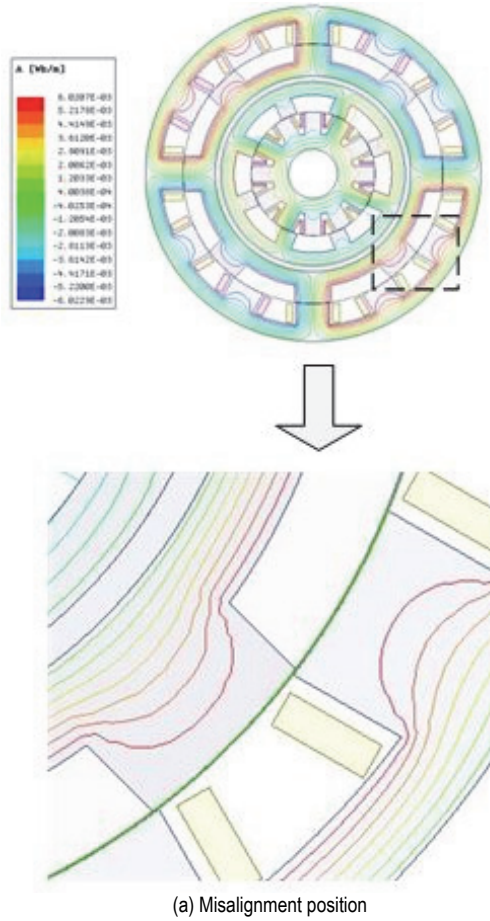

(a) Misalignment position

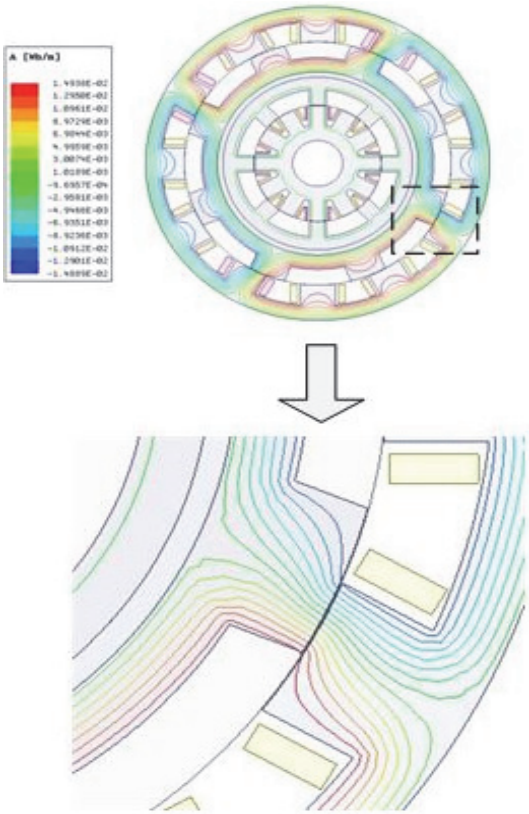

(b) Middle position

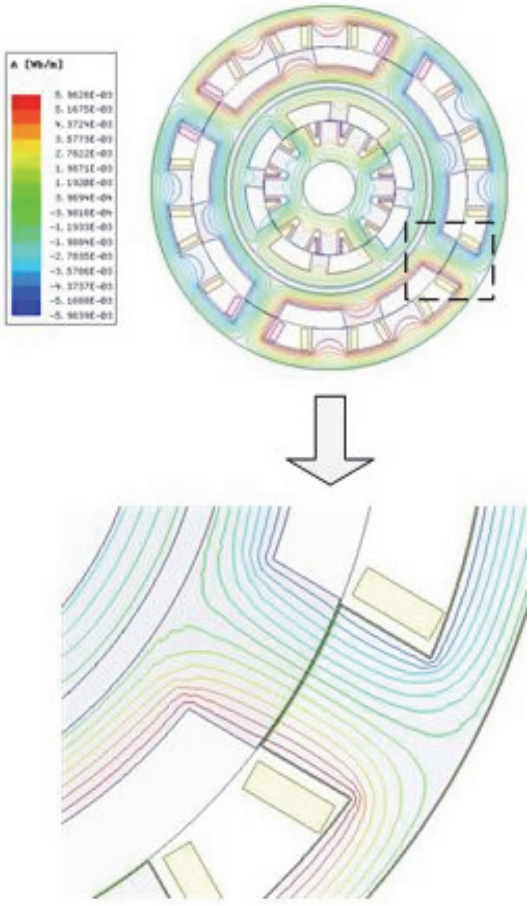

(c) Alignment position

Figure 6 Magnetic lines of force

As shown in Fig. 7, the magnetic density vector distribution diagram of the outer stator core of DDSSRG is shown, where A_{N1},A_{N2},A_{S1} and A_{S2} represent the two N poles

and two S poles of the tooth poles of the A-phase winding coil on the outer stator respectively. It can be seen that the magnetic vector starts from the A_{N1} and A_{N2} tooth poles, reaches the A_{S1} and A_{S2} tooth poles through the rotor, and then returns along the yoke of the outer stator core, forming four magnetic density directions with equal sizes. In a small area, the magnetic density is about 1.5 T.

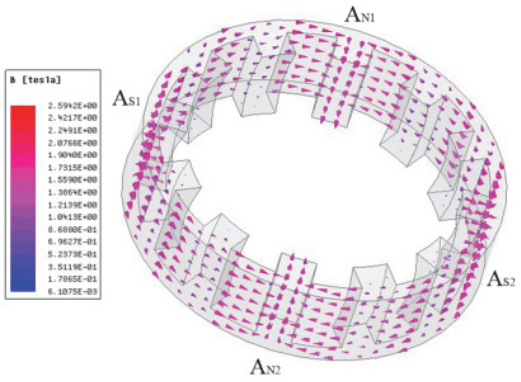

Figure 7 Flux density vector distribution of outer stator core

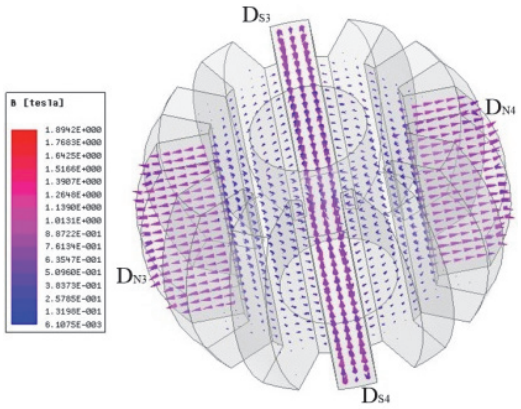

(a) Integral diagram of magnetic density vector distribution of inner stator core

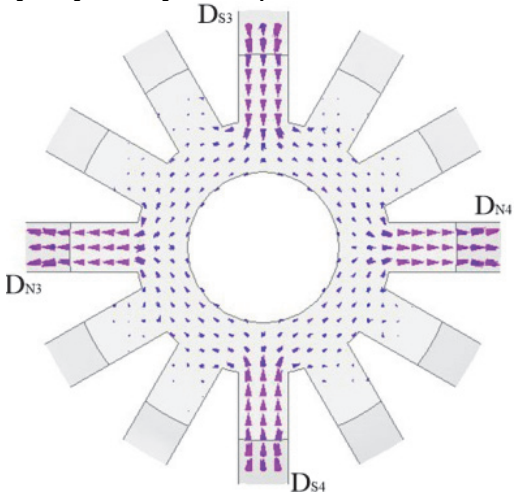

(b) Top view of inner stator core flux density vector

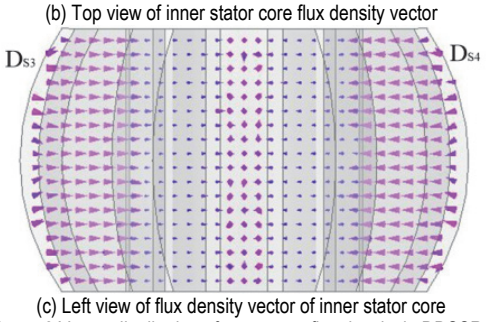

(c) Left view of flux density vector of inner stator core

Figure 8 Vector distribution of stator core flux density in DDSSRG

Fig. 8 shows the distribution of magnetic density vector of inner stator core, Fig. 8a D_{N3}, D_{N4}, D_{S3} and D_{S4} respectively represent the two N poles and two S poles of the tooth pole where the D-phase winding coil is located on the inner stator. The magnetic vector diverges from the D_{N3} and D_{N4} tooth poles, converges to the D_{S3} and D_{S4} tooth poles through the rotor, and then returns to the D_{N3} and D_{N4} tooth poles along the yoke of the inner stator core, forming four small regions with the magnetic density of about 0.5 T. Fig. 8b and Fig. 8c are the top view and left view of the inner stator core magnetic density vector, respectively.

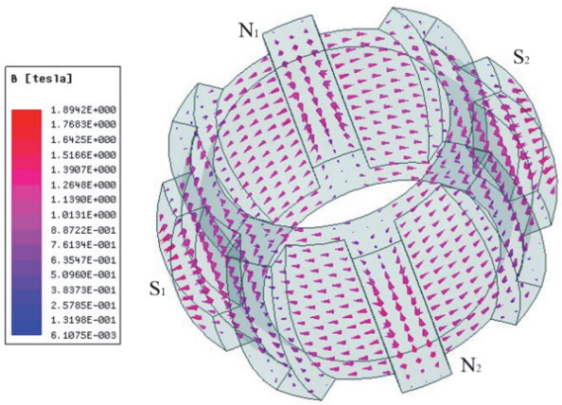

Figure 9 Distribution of magnetic flux density vector in the outer core of rotor

In Fig. 9 , the magnetic density vector distribution diagram of the outer core of the generator rotor is shown. The magnetic density at N_1 and N_2 corresponds to the magnetic density at A_{N1} and A_{N2} in Fig. 7, and the magnetic density at S_1 and S_2 corresponds to the magnetic density at A_{S1} and A_{S2} respectively. The magnetic density vector diverges from N_1 and N_2 poles to both sides, converges at S_1 and S_2, and then returns to N_1 and N_2 poles through the outer stator to form a closed magnetic circuit.

Fig. 10 shows the magnetic density vector distribution of the inner core of the rotor. The magnetic density at N_3 and N_4 in Fig. 11a corresponds to the magnetic density at D_{N3} and D_{N4} in Fig. 8a, and the magnetic density at S_3 and S_4 corresponds to the magnetic density at D_{S3} and D_{S4} respectively. Similarly, the flux density vector diverges from the N_3 and N_4 poles along the yoke, reaches S_3 and S_4, and then returns through the inner stator. Fig. 11b shows the top view of the flux density vector of the inner core of the rotor, and Fig. 11c shows the front view of the flux density vector of the inner core of the rotor.

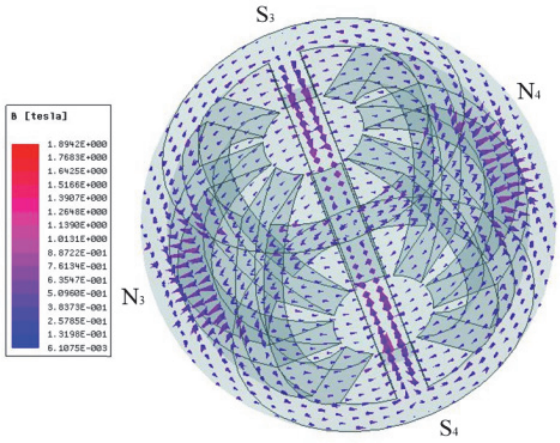

(a) Magnetic density vector distribution of inner core of rotor

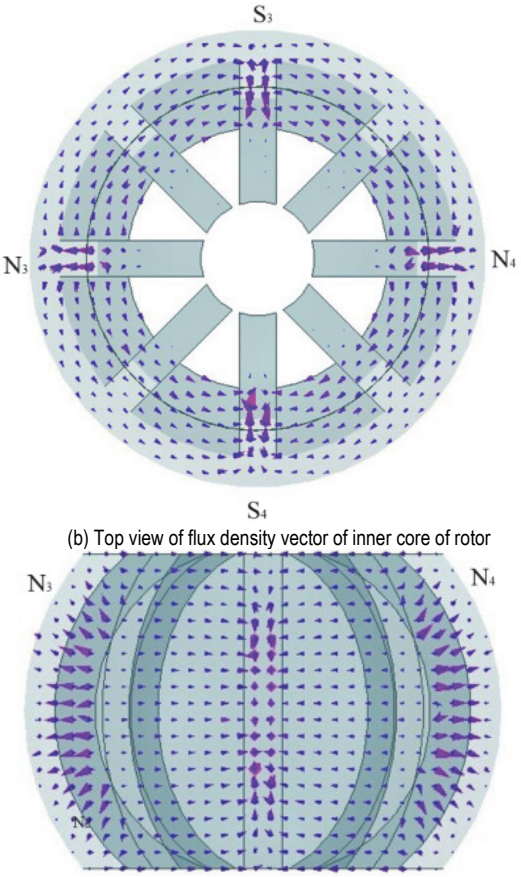

(b) Top view of flux density vector of inner core of rotor

(c) Front view of flux density vector of inner core of rotor

Figure 10 Vector distribution of magnetic density of generator rotor core

Six points in the core are selected as the research object to observe the change of the internal magnetic field of the generator core. The six selected points are shown in Fig. 11. The three points Ts_1, Ts_2 and Ts_3 in the figure represent the tooth tip, middle tooth and tooth root in the inner stator core, and the three points Tr_1, Tr_2 and Tr_3 respectively represent the tooth tip, middle tooth and tooth root of the inner core of the rotor.

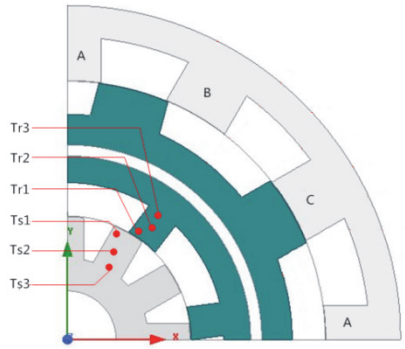

Figure 11 Node distribution of unit in DDSSRG core

In this paper, the transient simulation of the circuit magnetic field coupling is carried out for DDSSRG model, and the magnetic density of six points in Fig. 11 is simulated. It is stipulated that the generator rotation is counter clockwise, and the positive direction of the stator and rotor tooth pole flux is from the inner diameter to the outer diameter. The positive direction of the flux at the yoke of stator and rotor is counter clockwise. The rotor rotates 180° to obtain the waveform of magnetic density of each unit node with the rotor position.

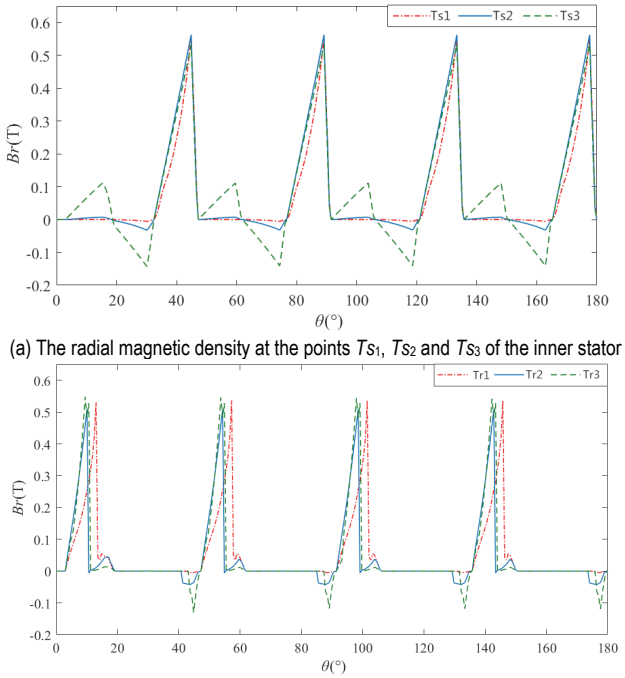

(a) The radial magnetic density at the points Ts_1, Ts_2 and Ts_3 of the inner stator

(b) Radial magnetic density at three points Tr_1, Tr_2 and Tr_3 inside the rotor

Figure 12 Radial magnetic density waveform

The radial magnetic density waveforms of stator inner teeth and rotor inner teeth are shown in Fig. 12. The amplitudes of three radial magnetic flux density components (Br) at Ts_1, Ts_2 and Ts_3 of inner stator teeth are around 0.52 t, and the magnetic density waveform pulsation at Ts_3 point is relatively large; the amplitude of three-point radial magnetic density br at the inner teeth of rotor is also around 0.52 t, which is consistent with the radial magnetic density component br of inner stator tooth.

4 STRUCTURAL OPTIMIZATION

Taguchi method [23-25] is an optimization method developed by Dr. Taguchi. At first, it is to improve the product quality, make the product quality stable, and minimize the impact on various interference. Later, Taguchi method optimization is gradually applied to all walks of life. As a local optimization method, Taguchi method can optimize the performance parameters of multiple motors at the same time. By using the designed orthogonal simulation experiment, a large number of experiments can be saved and the optimal parameter combination can be found as soon as possible. In this paper, Taguchi method is used to optimize DDSSRG.

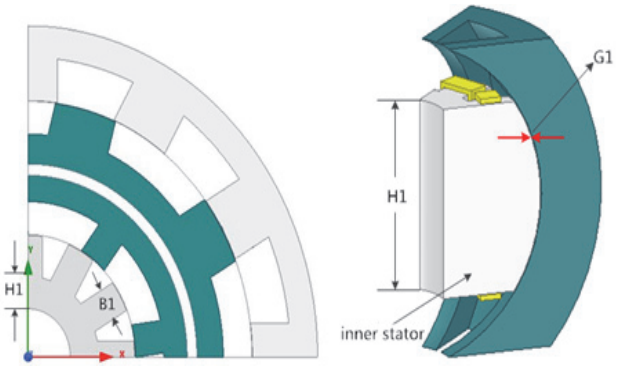

Figure 13 Schematic diagram of DDSSRG optimization parameters

In this paper, the internal stator parameters are optimized. The generator core loss is taken as the optimization objective. The inner stator core length L_1, stator pole width B_1, stator yoke height H_1 and internal air gap G_1 are selected as the analysis objects. The schematic diagram of optimization parameters is shown in Fig. 13.

The values of different optimization factors and levels are shown in Tab. 2.

Table 2 Different optimization factors and different level values

Horizontal factor	L_1	B_1	H_1	G_1
1	74.5	11.4	10.3	0.2
2	75.5	13.7	12.8	0.3
3	76.5	16.0	15.3	0.4

The orthogonal table can be generally expressed as $L_n(A^K)$, where n is the number of experiments; A is the number of horizontal values; and K is the number of optimization factors [26]. If a comprehensive experiment is to be carried out, a total of $3^4 = 81$ experiments are needed, which not only needs a lot of experimental time, but also has great requirements for the performance of computer hardware. By using Taguchi method, the simulation time can be saved by 80%.

The results of orthogonal experiment are shown in Tab. 3.

Table 3 $L_9(3^4)$ orthogonal table

Number of Experiments	G_1 / mm	B_1 / mm	H_1 / mm	L_1 / mm	P_{fe} / W
1	1	1	1	1	10.68
2	1	2	2	2	14.10
3	1	3	3	3	15.51
4	2	1	3	3	9.04
5	2	2	2	1	20.54
6	2	3	1	2	29.71
7	3	1	3	2	13.31
8	3	2	1	3	21.47
9	3	3	2	1	26.21

The variance value is used to represent the dispersion degree of the optimization target results of the motor under different optimization parameters and different levels. The proportion of the variance under a certain optimization parameter to the sum of the variance of all the optimization parameters can indicate the effect of the optimization parameter on the performance of the motor optimization target. The variance of the core length L_1 of the inner stator is as follows:

$$S_{L_1} = 3\sum_{i=1}^{3}\left[m_{L_1}\left(P_{fei}\right) - m\left(P_{fe}\right)\right]^2 \quad (1)$$

where $m_{L_1}\left(P_{fei}\right)$ is the average value of core loss of inner stator core length L_1 under the i-th horizontal variable and $m\left(P_{fe}\right)$ is the average value of core loss in 9 experiments.

The inner stator is very wide B_1, the yoke height is H_1, and the internal air gap is G_1. The calculation method of variance is the same.

The effects of various parameters on the experimental results are shown in Tab. 4.

It can be seen from Tab. 4 that under the current simulation level, the influence rate of inner stator pole width on core loss is the largest, and the influence of inner stator core length on motor performance is small. In order to simplify the optimization process, the parameters of inner stator width B_1, inner stator yoke height H_1 and internal air gap G_1 are selected to optimize.

Table 4 The influence of each parameter on the experimental results

Optimization parameters	Value	Impact rate / %
G_1 / mm	88.08	18.05
B_1 / mm	248.98	51.02
H_1 / mm	122.72	25.15
L_1 / mm	28.18	5.78
Total	487.96	100

The central composite design (CCD) method was used to fit the response surface. In this paper, CCD is used to design the test points: cube point (±1, ±1, ±1), center point (0, 0, 0) and axial point (±α, 0, 0), (0, ±α, 0), (0, 0, ±α). Taking three experimental factors for optimization, the value of α is 1.682, and a total of 19 experimental data points are investigated.

According to the CCD model theory, the level table of each factor variable is selected as shown in Tab. 5, and the experimental combination arrangement and experimental results are shown in Tab. 6.

Table 5 Experimental factor level table

level	B_1 / mm	G_1 / mm	H_1 / mm
$-\alpha$	11.87	0.23	11.61
–1	12.90	0.30	12.50
0	14.40	0.40	13.80
1	15.90	0.50	15.10
α	16.92	0.57	15.98

Table 6 CCD experiment arrangement and finite element simulation results

	B_1 / mm	G_1 / mm	H_1 / mm	P_{fe}
1	–1	–1	–1	15.48
2	1	–1	–1	26.47
3	–1	–1	1	9.18
4	1	–1	1	25.17
5	–1	1	–1	12.85
6	1	1	–1	19.26
7	–1	1	1	7.51
8	1	1	1	20.57
9	–1.682	0	0	6.89
10	1.682	0	0	28.63
11	0	0	–1.682	22.21
12	0	0	1.682	15.64
13	0	–1.682	0	19.04
14	0	1.682	0	11.08
15	0	0	0	21.48
16	0	0	0	22.08
17	0	0	0	21.12
18	0	0	0	21.62
19	0	0	0	21.07

The simulation results were calculated by Design-Expert, and the experimental results are fitted by multivariate two-dimensional model, and the model is modified after eliminating the insignificant variables

$$Y = 21.47 + 6.08X_1 - 1.66X_2 - 2.16X_3 + 1.46X_1X_2 - \\ -0.94X_1X_3 + 0.45X_2X_3 - 1.30X_1^2 - 0.89X_2^2 - 2.25X_3^2 \quad (2)$$

where Y is core loss of inner stator, X_1 is the inner determiner is very wide B_1, X_2 is Inner yoke height H_1 and X_3 is internal air gap G_1.

In order to evaluate the fitting degree of the models, variance analysis was used to evaluate the three fitting models, and the significance of each model was determined by *p*-value. It can be seen from Tab. 4 that the *p*-value of the fitting model for core loss P_{fe} is less than 0.05, indicating that the model fitting result is good and has statistical significance. The *p*-value of the pseudo loss value of the model is greater than 0.05, explaining that the error of the fitting result is small and the error is not significant. The correction coefficient of regression equation can evaluate the model under the influence of the number of independent variables, and determine whether the connection between experimental factors and response is significant. The results of Design-Expert statistical analysis show that the correction coefficient of core loss is 0.9949, which is greater than 0.9. The relationship between experimental factors and response is significant. The model fully represents the relationship between experimental factors and response.

According to the above analysis, the three-dimensional response curves between the core loss of the stator and the structural parameter variables are drawn, as shown in Fig. 14.

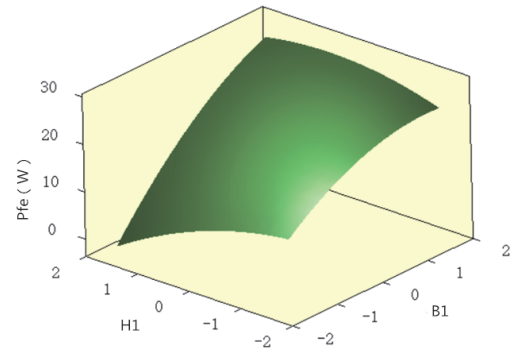

(a) Response surface of iron loss of internal determiner varying with H_1, B_1

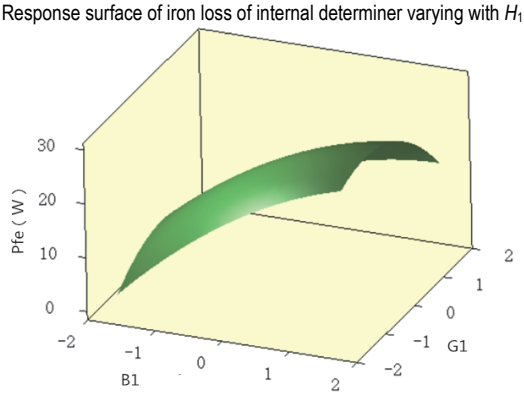

(b) Response surface of iron loss of internal determiner varying with B_1, G_1

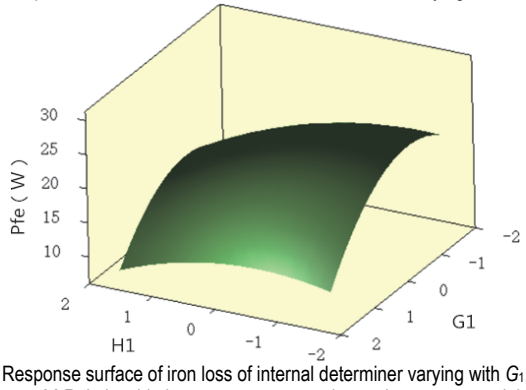

(c) Response surface of iron loss of internal determiner varying with G_1, H_1

Figure 14 Relationship between response value and parameter variables

The horizontal axis in Fig. 14 shows the coding value of the parameter variable. It can be seen from Fig. 14a and Fig. 14b that the change trend of P_{fe} response surface of inner stator iron loss with the inner stator very wide B_1 is the most obvious, P_{fe} increases with the increase of B_1, and the interaction between internal air gap G_1 and B_1 is not significant. Fig. 14c shows that P_{fe} decreases with the increase of inner stator yoke height H_1 and G_1, and the variation range is relatively small.

The inner stator core loss response surface model of the generator is further optimized by Design-Expert software. The optimized structure dimensions are as follows: the inner stator pole width B_1 is 13.9 mm, the inner stator yoke height H_1 is 14.6 mm, and the internal air gap G_1 is 0.43 mm.

5 EXPERIMENTAL VERIFICATION

As shown in Fig. 15, an experimental platform of DDSSRG system is built. The experimental platform includes wind turbine simulation and power generation system. In the wind turbine simulation part, a servo motor is used to drive the generator to rotate, and the wind turbines with different speeds are simulated to provide mechanical energy for the generator. When the wind direction changes, the power generation efficiency of the generator is maintained under the joint action of deflection turntable and deflection measuring device. During the operation of the generator, the external excitation voltage source Us always exists, so as to ensure the stability of the generator excitation voltage. Under this excitation mode, the power generation circuit and the excitation circuit do not interfere with each other and are independent of each other. The excitation voltage does not change with the fluctuation of the output voltage, but can also be adjusted according to the demand, Self adjust excitation voltage or output voltage. The excitation voltages of the internal generator and the external generator in the power generation system are 15 V and 36 V respectively, so as to ensure the stability of the generator output performance. STM32F103C8T6 is selected as the main control chip, and the deflection type double stator SRG is responsible for converting mechanical energy into electrical energy output under the driving of prime mover.

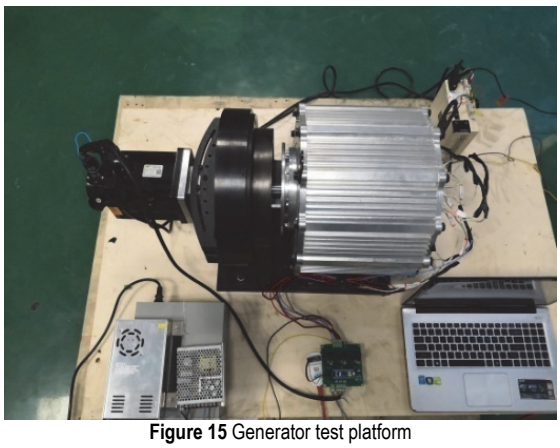

Figure 15 Generator test platform

The output voltage of the generator is tested, and the output voltage waveform of DDSSRG as shown in Fig. 16 is obtained.

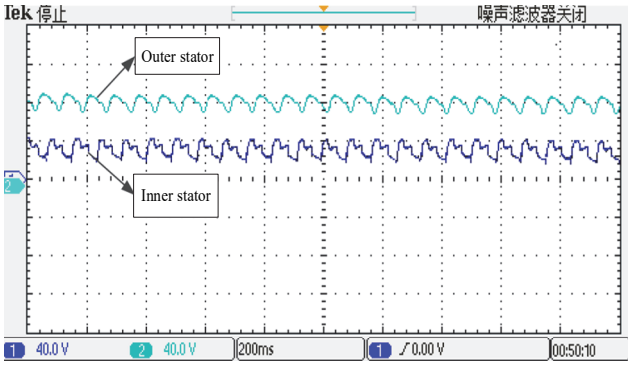

(a) Output voltage of inner and outer stator of generator

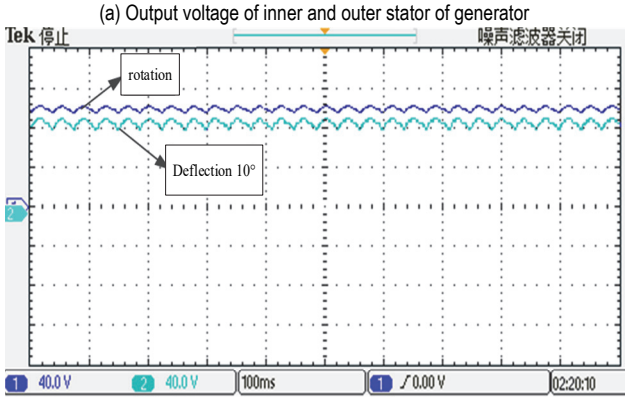

(b) Output voltage of generator under rotation and deflection

Figure 16 Output voltage waveform of DDSSRG

Fig. 16a is the waveform diagram of output voltage of internal generator and external generator at the speed of 100 r/min. It can be seen that the amplitude of output voltage of internal stator fluctuates up and down 32 V, and the amplitude of output voltage of outer stator fluctuates around 80 V. As shown in Fig. 16b, when the rotation speed is 200 r/min the output voltage amplitude of external generator in rotation state fluctuates at 96 V, and the output voltage amplitude fluctuates between 85 V at 10° deflection. It can be seen from the figure that when the generator deflects, the amplitude of output voltage decreases slightly and the ripple of waveform increases slightly, but the overall output waveform changes little. From the experimental results, it can be concluded that the generator can still maintain good output characteristics in the deflection state.

6 CONCLUSION

To better meet the requirements of wind power generation, DDSSRG is proposed in this paper, and the magnetic field of the generator is analyzed. In order to improve the working efficiency of DDSSRG, the stator core loss is selected as the optimization objective, and the response surface method is applied to optimize its structure, and the optimal structural parameters are obtained through analysis.

Finally, the experimental platform is built. The wind speed simulation is realized by driving the generator with prime mover. The output voltage of inner stator, outer stator, rotation and deflection state of generator is measured by selecting separate excitation mode. Through the analysis of experimental results, the correctness and practicability of the generator structure are further verified.

Acknowledgements

This work is supported by the National Natural Science Foundation of China (No. 51877070, U20A20198, 51577048), the Natural Science Foundation of Hebei Province of China (No. E2021208008, E2018208155), the Talent Engineering Training Support Project of Hebei Province (A201905008), the National Engineering Laboratory of Energy-saving Motor & Control Technique, Anhui University (No. KFKT201901).

7 REFERENCES

[1] Liu, X., Park, K., & Chen, Z. (2014). A Novel Excitation Assistance Switched Reluctance Wind Power Generator. *IEEE Transactions on Magnetics*, *50*(11), 1-4. https://doi.org/10.1109/tmag.2014.2327798

[2] Castro Teixeira, V. S., Filho, E. R., & Santos Barros, T. A. (2015). Design, optimization and analysis of the axial C-core Switched Reluctance Generator for wind power application. *2015 International Conference on Renewable Energy Research and Applications (ICRERA)*, 833-837. https://doi.org/10.1109/icrera.2015.7418528

[3] De Castro Teixeira, V. S., Barros, T. A. D. S., & Moreira, A. B. (2018). Methodology for the Electromagnetic Design of the Axial-Flux C-Core Switched Reluctance Generator. *IEEE Access*, *6*, 65463-65473. https://doi.org/10.1109/access.2018.2878146.

[4] Wang, D., Shao, C., & Wang, X. (2016). Performance Characteristics and Preliminary Analysis of Low Cost Tubular Linear Switch Reluctance Generator for Direct Drive WEC. *IEEE Transactions on Applied Superconductivity*, *26*(7), 1-5. https://doi.org/10.1109/tasc.2016.2599920

[5] Choi, D. W., Byun, S. I., & Cho, Y. H. (2014). A study on the maximum power control method of switched reluctance generator for wind turbine. *IEEE Transactions on Magnetics, 50*(1), 1-4. https://doi.org/10.1109/tmag.2013.2274174

[6] Xiang, Q., Sun, Y., & Zhang, X. (2011). Optimization design of the bearingless switched reluctance motor based on SVM and GA. *Proceedings of the 30th Chinese Control Conference*, 1472-1475.

[7] Omekanda, A. M. (2006). Robust torque and torque-per-inertia optimization of a switched reluctance motor using the Taguchi methods. *IEEE Transactions on Industry Applications*, *45*(2), 473-478. https://doi.org/10.1109/tia.2006.870031

[8] Zuo, S., Liu, Z., & Hu, S. (2020).Vibration reduction of switched reluctance motor under static eccentricity with optimised current harmonic. *IET Electric Power Applications*, *14*(8), 1480-1487. https://doi.org/10.1049/iet-epa.2019.1044

[9] Cao, G., Fang, J., & Huang, S. (2014). Optimization Design of the Planar Switched Reluctance Motor on Electromagnetic Force Ripple Minimization. *IEEE Transactions on Magnetics*, *50*(11), 1-4. https://doi.org/10.1109/tmag.2014.2323481

[10] Yildiz, A., Polat, M., & Özdemir, M. T. (2018). Design Optimization of Inverted Switched Reluctance Motor using Ant Colony Optimization Algorithm. *2018 International Conference on Artificial Intelligence and Data Processing (IDAP)*, 1-6. https://doi.org/10.1109/idap.2018.8620923

[11] Jiang, J. W., Peng, F., & Bilgin, B. (2017). Optimisation-based procedure for characterising switched reluctance motors.*IET Electric Power Applications*, *11*(8), 1366-1375. https://doi.org/10.1049/iet-epa.2017.0072

[12] Asgar, M., Afjei, E., & Torkaman, H. (2015). A New Strategy for Design and Analysis of a Double-Stator

Switched Reluctance Motor: Electromagnetics, FEM, and Experiment. *IEEE Transactions on Magnetics*, *51*(12), 1-8. https://doi.org/10.1109/tmag.2015.2465307

[13] Gouda, E. & Salah H. M. (2019). A proposed design, implementation and control of doubly fed switched reluctance motor. *CES Transactions on Electrical Machines and Systems*, *3*(1), 101-106. https://doi.org/10.30941/cestems.2019.00014

[14] Lee, C. H. T., Chau, K. T., & Liu, C. (2014). Mechanical Offset for Torque Ripple Reduction for Magnetless Double-Stator Doubly Salient Machine. *IEEE Transactions on Magnetics*, *50*(11), 1-4. https://doi.org/10.1109/tmag.2014.2320964

[15] Guo, T., Schofield, N., & Emadi, A. (2016). Double Segmented Rotor Switched Reluctance Machine with Shared Stator Back-Iron for Magnetic Flux Passage. *IEEE Transactions on Energy Conversion, 31*(4), 1278-1286. https://doi.org/10.1109/tec.2016.2600178

[16] Li, Z., Yu, X., & Qian, Z. (2020). Generation Characteristics Analysis of Deflection Type Double Stator Switched Reluctance Generator. *IEEE Access*, *8*, 196175-196186. https://doi.org/10.1109/access.2020.3034467

[17] Abbasian, M., Moallem, M., & Fahimi, B. (2010). Double-Stator Switched Reluctance Machines (DSSRM): Fundamentals and Magnetic Force Analysis. *IEEE Transactions on Energy Conversion*, *25*(3), 589-597. https://doi.org/10.1109/tec.2010.2051547

[18] Cosoroaba, E., Bostanci, E., & Li, Y. (2017). Comparison of winding configurations in double-stator switched reluctance machines. *IET Electric Power Applications*, *11*(8), 1407-1415. https://doi.org/10.1109/icelmach.2014.6960305

[19] Cheng, Y., Li, D., & Kong, W. (2018). Electromagnetic Design of a Large-Scale Double-Stator Direct Driving HTS Wind Generator. *IEEE Transactions on Applied Superconductivity*, *28*(4), 1-5. https://doi.org/10.1109/tasc.2018.2803265

[20] Liu, Y., Niu, S., & Ho, S. L. (2015). Design and Analysis of a New HTS Double-Stator Doubly Fed Wind Generator. *IEEE Transactions on Applied Superconductivity*, *25*(3), 1-4. https://doi.org/10.1109/tasc.2014.2366458

[21] Zhang, B., Wu, F., Zhang, Z., Wei, Z., & Xi, J. (2019). 3D Magnetic Field Finite Element Analysis of Dual-Stator PM Spherical Motor. *2019 Chinese Control and Decision Conference (CCDC)*, 5616-5620. https://doi.org/10.1109/ccdc.2019.8832404

[22] Wang, W. & Zhang, H. (2020). The Analysis of Magnetic Field and Electromagnetic Force for Transverse Flux Permanent Motor. *2020 Chinese Automation Congress (CAC)*, 5890-5895. https://doi.org/10.1109/cac51589.2020.9326627

[23] Kim, S.-I., Lee, J.-Y., Kim, Y.-K., Hong, J.-P., Hur, Y., & Jung, Y.-H. (2005). Optimization for reduction of torque ripple in interior permanent magnet motor by using the Taguchi method. *IEEE Transactions on Magnetics*, *41*(5), 1796-1799.

[24] Hwang, C., Chang, C., & Liu, C. (2013). A Fuzzy-Based Taguchi Method for Multiobjective Design of PM Motors. *IEEE Transactions on Magnetics*, *49*(5), 2153-2156. https://doi.org/10.1109/tmag.2013.2242854

[25] Guo, Y., Si, J., Gao, C., Feng, H., & Gan, C. (2019). Improved Fuzzy-Based Taguchi Method for Multi-Objective Optimization of Direct-Drive Permanent Magnet Synchronous Motors. *IEEE Transactions on Magnetics*, *55*(6), 1-4. https://doi.org/10.1109/tmag.2019.2897867

[26] Gao, Z. Y., Xie, J., & Wang, S. M. (2014). Optimization Design of Transverse Flux Permanent Generator Based on Response Surface Method. *Advanced Materials Research*, *936*, 2135-2139. https://doi.org/10.4028/www.scientific.net/amr.936.2135

Contact information:

Zhe QIAN, PhD
Anhui University,
National Engineering Laboratory of Energy-saving Motor & Control Technique,
Hefei, Anhui 230601, China
E-mail: zheqian2@163.com

Xueting WANG
Hebei University of Science and Technology,
School of Electrical Engineering,
Shijiazhuang, Hebei 050018, China
E-mail: wangxueting119@163.com

Zheng LI, PhD, Professor
(Corresponding author)
Hebei University of Science and Technology,
School of Electrical Engineering,
Shijiazhuang, Hebei 050018, China
E-mail: Lzhfgd@163.com

Xuze YU
Hebei University of Science and Technology,
School of Electrical Engineering,
Shijiazhuang, Hebei 050018, China
E-mail: aaliuyf1@qq.com